Controlling Size, Amount, and Crystalline Structure of Nanoparticles Deposited on Graphenes for Highly Efficient Energy Conversion and Storage

Bong Gill Choi[a] and Ho Seok Park*[b]

A facilitated electrochemical reaction at the surface of electrodes is crucial for highly efficient energy conversion and storage. Herein, various nanoparticles (NPs) including Au, Pt, Pd, Ru, and RuO$_2$, were synthesized in situ and directly deposited on the ionic liquid (IL)-functionalized reduced graphene oxides (RGOs) in a controlled manner. The size, amount, and crystalline structures of discrete NPs were readily controlled, giving rise to enhanced methanol oxidation and pseudocapacitance. The well-defined nanostructure of decorated NPs and the favorable interaction between ILs and RGOs (or NPs) facilitated the electrochemical reaction, where NPs acted as electrocatalysts for energy conversion and played the role of redox-active electrodes for energy storage.

Introduction

At the central part of energy conversion and storage systems, such as fuel cells, solar cells, batteries, and supercapacitors (SCs), are electrode materials, which transfer electrons generated at the interfaces.[1,2] Along with a facilitated electronic conduction through the electrodes, efficient redox reactions occurring at the electrode/electrolyte interface are highly desirable for high performance electrochemical devices.[3] Moreover, the electrode materials used as electrocatalysts contribute to enhancing the redox reaction of chemicals such as hydrogen and methanol for energy conversion, whereas the electroactive materials directly participate in the faradaic process occurring at the surface of electrode for energy storage. For a breakthrough in energy conversion and storage, conventional electrodes should be replaced by a nanostructured material, which have a large accessible area, short diffusion lengths, and an unusual quantum effect.[4,5]

Recently, graphene-based nanohybrids have received considerable attention as an emerging class of nanomaterials for multifunctional systems owing to their potential applications in catalysis, optoelectronics, sensors, hydrogen storage, energy conversion, and storage.[6,7] Graphene itself can also be a functional nanomaterial due to its large surface area, high electrical and thermal conductivity, and chemical and mechanical stability.[8,9] More importantly, hybridization with other nanoparticles (NPs) has been suggested as a useful and alternative technology in terms of offering a synergistic effect and expanding the applicative fields of graphenes, especially for energy conversion and storage.[10] The integration of carbon nanomaterials and NPs is governed by three main issues: the size, uniformity, and amount of the decorated NPs must be controlled to produce high performance hybrids.[11] To date, direct (in situ) deposition of NPs on the surface of graphenes has been widely used to synthesize such nanohybrids, as the uniform distribution of discrete NPs is readily achieved in a controllable manner.[12] Another important challenge, the transformation into different crystalline structures, must be resolved to accomplish the optimum performance of electrochemical systems.

Ionic liquids (ILs) have been studied extensively in recent years for the functionalization of carbon nanomaterials starting with the fabrication of bucky gels as reported by Aida's group.[13] The electrochemical applications of IL-functionalized carbon nanotubes (CNTs) were promoted by the unique properties of ILs, including high ionic conductivity and electrochemical stability.[14] Moreover, various NPs have been synthesized in situ and directly deposited on CNTs using ILs as the active sites.[11,15] Inspired by these intensive efforts on the functionalization of CNTs by ILs,[14] this concept has been applied to the functionalization of graphenes,[16,17] but there are still very few reports regarding the different chemistries and geometries of graphenes and CNTs. For instance, the utilization of ILs has been limited to the enhancement of the dispersion of graphenes and to the deposition of Pt NPs.[16–18] Neither the versatile and controllable synthesis of NPs nor the fundamental understanding about the correlation between structure and property of NPs for energy conversion and storage have been explored.

Herein, NPs including Au, Pt, Pd, Ru, and crystalline RuO$_2$ are synthesized in situ and directly deposited on the IL-functionalized reduced graphene oxides (RGOs) for highly efficient

[a] B. G. Choi
Department of Chemical & Biomolecular Engineering (BK21)
Korea Advanced Institute of Science and Technology
Daejeon 305-701 (Republic of Korea)

[b] Prof. Dr. H. S. Park
Department of Chemical Engineering
College of Engineering
Kyung Hee University
Yongin-si 446-701 (Republic of Korea)

Supporting Information for this article is available on the WWW under http://dx.doi.org/10.1002/cssc.201100565.

energy conversion and storage. In particular, the size, amount, and crystalline structures of uniform NPs are readily regulated by controlling synthetic parameters through solution chemistry. As a result, the as-obtained hybrids showed 43 and 25% higher performance compared to conventional RGO-based materials for energy conversion and storage.

Results and Discussion

The synthesis of NP/IL-RGO hybrids is illustrated in Figure 1. The synthetic route is based on the supramolecular assembly of RGOs with 1-butyl-3-methylimidazolium tetrafluoroborate ([bmim][BF$_4$]) ILs, which is a facile, effective, and straightforward method for the modification of graphene. The GOs, prepared by using a modified Hummers method,[19] were functionalized with ILs through solution chemistry. After the chemical reduction, IL-RGOs remain dispersible and stable in aqueous solutions. The functionalization of RGOs by ILs was attributed
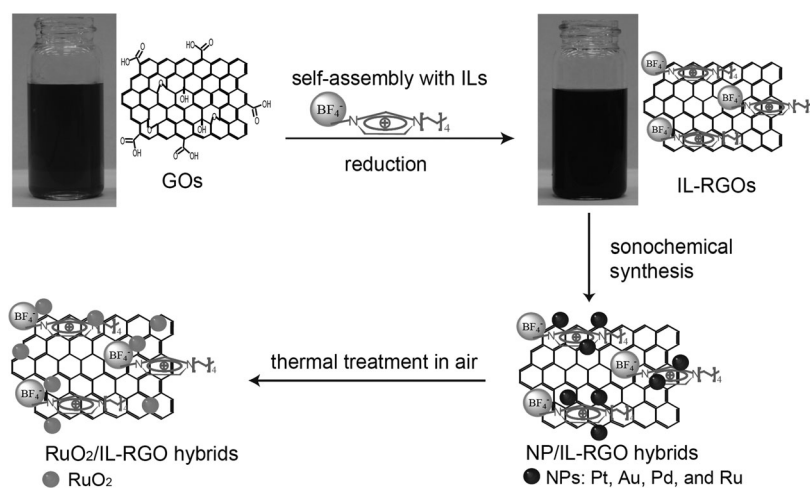
$\tilde{\nu}_{H_2O, ads.}$, 1396 cm^{-1} for $\tilde{\nu}_{O-H, deform.}$, 1227 cm^{-1} for $\tilde{\nu}_{C-OH}$, and 1089 cm^{-1} for $\tilde{\nu}_{C-O, stretch}$.[20] The characteristic oxygen moiety bands of IL-RGOs exhibited lower intensities compared to those of GOs. In addition, IL-RGOs revealed the emergence of the strong bands at 1569 cm^{-1} for $\tilde{\nu}_{CH_3-N}$, 1167 cm^{-1} for $\tilde{\nu}_{imidazolium ring}$, and 1053 cm^{-1} for $\tilde{\nu}_{BF_4}$, indicating the presence of ILs.[21] This result was supported by the C 1s XPS spectra. The C 1s spectrum of GOs could be deconvoluted into four peaks: O−C=O (289.1), C=O (288), C−O (286.5), and C−C (284.5 eV), which is in accordance with a previous report.[22] In comparison to the C 1s spectrum of GOs, IL-RGOs clearly showed an increase in the intensity of the C−C peak and a corresponding decrease in the intensity of the C−O peak, imparting the restoration of large domains of π-conjugation in the structure of IL-RGOs.

The quality of NPs deposited on IL-RGOs was evaluated by means of TEM, XRD, and XPS as shown in Figure 2. Discrete Pt NPs were uniformly distributed on the surfaces of fully exfoliated IL-RGOs. High resolution (HR)-TEM images clearly show the narrow size distribution of NPs with an average diameter of 2.1 ± 0.17 nm, which was calculated by measuring diameters of > 100 samples. In contrast, RGOs prepared without the modification of ILs showed irregular size and non-uniform, broad distribution of Pt NPs with an average diameter of approximately 4.4 ± 0.62 nm (see the Supporting Information, Figure S2). These results indicate that the ILs regulated the growth of NPs through electrostatic interactions, giving rise to high quality hybrid materials. The molecular structures of
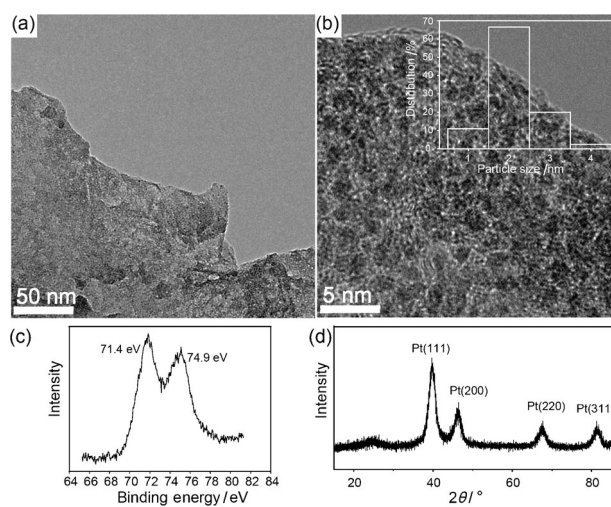

Figure 1. Fabrication process of NP/IL-RGO hybrids and the post-thermal treatment for the transformation of RuO$_2$ crystalline structures.

to the π–π stacking and cation–π interactions between the restored conjugated structures of RGOs and imidazolium cations of ILs.[13–17] The anions of the ILs coated on the surface of RGOs can offer activated sites to assist the growth and deposition of NPs while preventing the reaggregation of the RGOs in an aqueous solution.[15] NP precursors, interacting with ILs coated on the surface of RGOs, were nucleated by ultrasound irradiation, and then nanocrystals were grown on the surface of IL-RGOs. To apply nanohybrids in capacitive electrodes, crystalline structures of RuO$_2$/IL-RGO were prepared by post-thermal treatment of Ru/IL-RGO hybrids. Furthermore, the as-obtained NPs/IL-RGOs were readily dispersed in aqueous solutions due to the hydrophilic nature of the ILs.

The functionalization and reduction of RGOs was confirmed by means of FTIR and X-ray photoelectron spectroscopy (XPS, see the Supporting Information, Figure S1). The characteristic bands of the FT-IR spectra of GO were assigned as follows: 3431 cm^{-1} for $\tilde{\nu}_{O-H, stretch}$, 1720 cm^{-1} for $\tilde{\nu}_{C=O}$, 1627 cm^{-1} for

Figure 2. a, b) TEM images of Pt/IL-RGO (inset shows size distribution for Pt/IL-RGO hybrids.). c) XPS and d) XRD spectra of Pt/IL-RGO hybrids.

Pt/IL-RGO nanohybrids were further investigated by using XPS and XRD data. Two characteristic peaks at 74.9 eV for Pt (4f$_{5/2}$) and 71.4 eV for Pt (4f$_{7/2}$) in XPS spectra of the hybrids are indicative of the presence of a metallic form of Pt NPs.[23] Moreover, the XRD pattern of Pt/IL-RGO hybrids was assigned to the face-centered cubic structure, which consists of four main peaks corresponding to the (111), (200), (220), and (311) planes, indicating the construction of nanocrystalline structures.[24] Along with controlling the size, the amount of Pt NPs deposited on IL-RGO hybrids was manipulated by changing the concentration of the NP precursors. As shown in the scanning TEM (STEM) images (Figure 3), the Pt signal of the hybrid relative to the C signal increased with respect to the concentration of precursors. This result was confirmed by thermal gravimetric analysis (TGA) data (see the Supporting Information, Figure S3).

The versatility of this strategy was confirmed by the synthesis of other NP/IL-RGO hybrids, including Au, Pd, and Ru. Au, Pd, and Ru NPs were directly nucleated onto the IL-RGO surfaces using a procedure identical to that for Pt/IL-RGO hybrids (Figure 4). Three NPs were readily nucleated and simultaneously grown on the binding sites of a IL-functionalized RGO surface. The average diameters were calculated to be 4.3 ± 0.42, 2.3 ± 0.26, and 1.9 ± 0.21 nm for Au/IL-RGO, Pd/IL-RGO, and Ru/IL-RGO, respectively. The identity of the NPs was confirmed by means of energy dispersive X-ray spectroscopy (EDX, see the Supporting Information, Figure S4). The morphologies and sizes of the NPs were dependent on the type of NPs, because of the interactions between NPs and IL-RGOs and the growth kinetics of NPs.[11] The superior features of Pt/IL-RGO nanohybrids arising from the control in the size and uniformity were demonstrated by applying them to the electrooxidation of methanol. Methanol oxidation was chosen in this work as a model redox reaction because the electrocatalysis for this reaction is required in high performance fuel cells.[25] All of the Pt/IL-RGO and Pt/RGO nanohybrids were prepared following identical protocols and then investigated by electrochemical measurements as shown in Figure 5. In addition, commercial Pt black (E-Tec) was used as a control sample. The electrochemical surface areas (ESAs) of E-tec, Pt/RGO, and Pt/IL-RGO catalysts were evaluated by performing cyclic voltammetry (CV) measurements using the hydrogen adsorption–desorption method and Equation (1):[26]
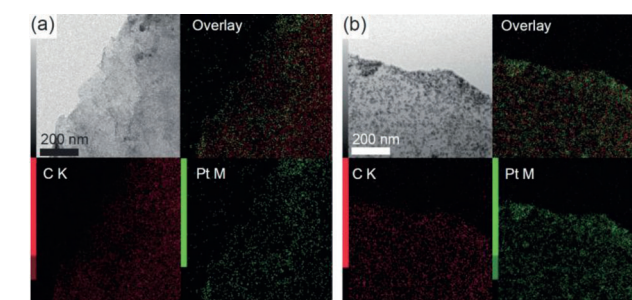

Figure 3. STEM images of Pt/IL-RGO hybrids at the concentration of a) 2 and b) 4×10^{-3} mmol of Pt precursors. Top left panel corresponds to TEM image, top right panel to an overlay image, bottom left image to carbon signal, and bottom right image to the Pt signal.

$$ESA = Q_H / (L_{Pt} \times 0.21) \tag{1}$$

in which Q_H is the charge passed through H-adsorption, L_{Pt} is Pt loading (mg cm^{-2}) in the electrode, and 0.21 (mC cm^{-2}) is the charge required to oxidize a monolayer of H_2 on a Pt surface. The ESA of Pt/IL-RGO was calculated to be 237 cm^2 mg^{-1}, which was larger than that of E-Tec (162) and Pt/RGO (181 cm^2 mg^{-1}). The large ESA of the Pt/IL-RGO was responsible for the facilitated electrocatalytic reactions because of the easy accessibility to the reaction sites and the large surface area of discrete NPs. Figure 5b shows typical CVs of the electrocatalysts for the electrooxidation of methanol in a N_2-saturated so-
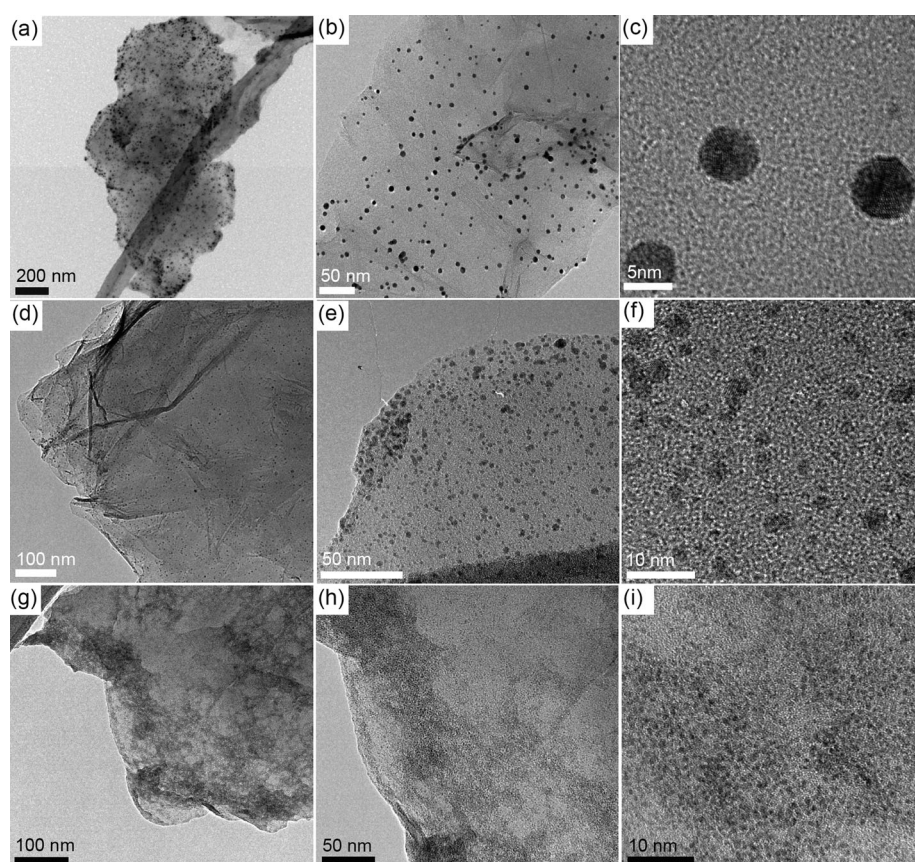

Figure 4. TEM images of a–c) Au/IL-RGO hybrids, d–f) Pd/IL-RGO hybrids, and g–i) Ru/IL-RGO hybrids.
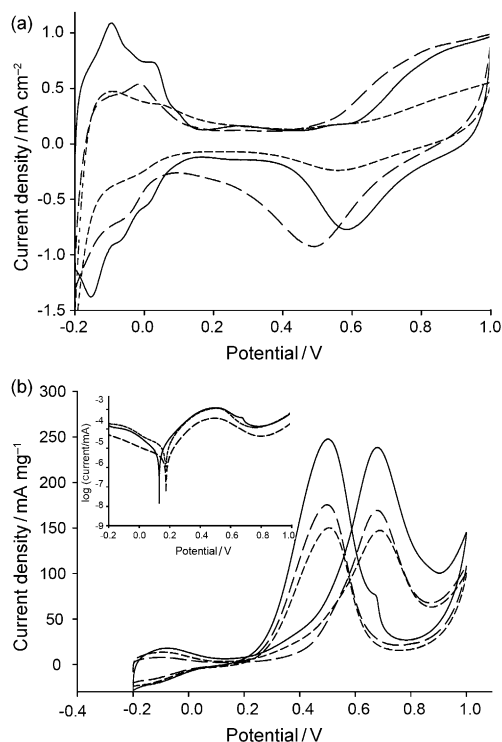
Figure 5. CV curves of Pt/IL-RGO (———), Pt/RGO (– – –), and E-Tec (- - - -) electrocatalysts at 50 mV s^{-1} in a) N$_2$-saturated 0.5 M H$_2$SO$_4$ and b) N$_2$-saturated 0.5 M CH$_3$OH/1 M H$_2$SO$_4$ at 50 mV s^{-1}. Inset is a Tafel plot for the Pt/IL-RGO, Pt/RGO, and E-Tec electrocatalysts obtained from the CV data.

Figure 6. a) STEM images of RuO$_2$/RGO-IL hybrids. Top left panel corresponds to TEM image, top right panel to the carbon signal, bottom left image to the Ru signal, and bottom right image to the oxygen signal. b) XRD pattern of RuO$_2$/RGO-IL hybrids.

lution of 0.5 M H$_2$SO$_4$/1 M CH$_3$OH at a scan rate of 50 mV s^{-1}. The peak current of Pt/IL-RGO for the electrooxidation of methanol was 238 mA mg$^{-1}_{Pt}$, which is approximately 43 and 63% higher than that of Pt/RGO (167) and E-Tec (146 mA mg$_{Pt}^{-1}$), respectively. Furthermore, the onset potential of Pt/IL-RGO for the electrooxidation of methanol appeared at 0.131 V, which is lower than that of Pt/RGO (0.176) and E-Tec (0.180 V) due to the interaction of ILs between the NPs and RGOs. It is worth noting that the elaborate performance of Pt/IL-RGO nanohybrids for the electrocatalysis was attributed to the well-defined structures, such as small size and narrow size distribution, of discrete NPs.

In this study, RuO$_2$/IL-RGO hybrids were chosen as electrode materials for electrochemical energy storage, as both RuO$_2$ and RGOs are currently regarded as potential materials for pseudocapacitors and electrical double layer capacitors (EDLCs), respectively.[27–29] However, the control in the crystalline structures of RuO$_2$ deposited on RGOs has been too elusive for understanding the effect of molecular structures on energy-storage performance. Crystalline structures of RuO$_2$ deposited on IL-RGO were readily obtained through the post-thermal treatment of Ru/IL-RGO. As shown in Figure 6, crystalline RuO$_2$/IL-RGO hybrids showed the rutile phase through transformation from metallic Ru. In an analogous manner to Pt/IL-RGO, RuO$_2$ NPs were uniformly deposited on the surface of IL-functionalized RGOs as shown in STEM and SEM images (see the Supporting Information, Figure S5).
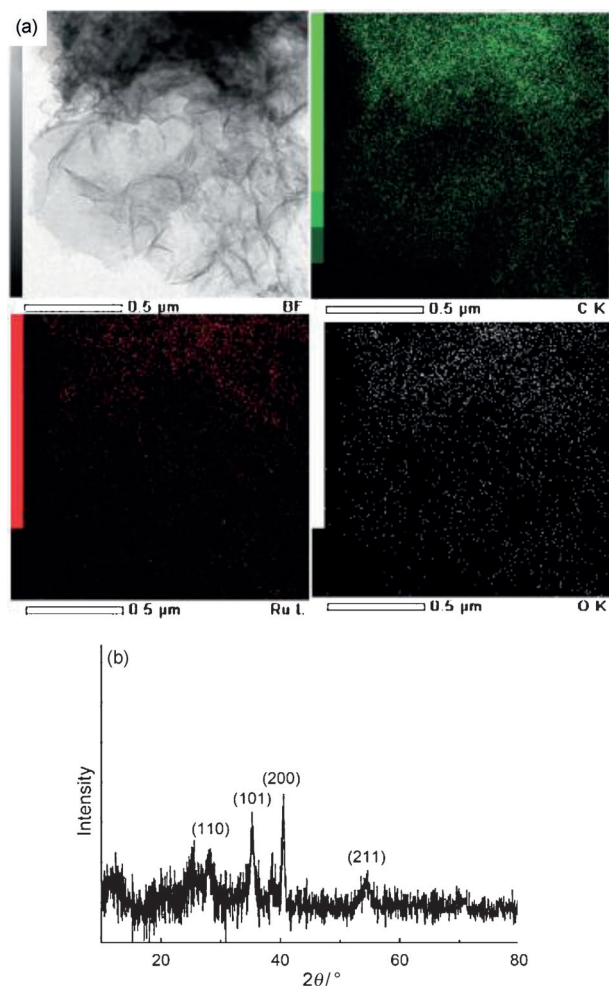
As shown in the cell configuration of Figure 7 a, we used RuO$_2$/IL-RGO hybrids as electrodes, 1 M H$_2$SO$_4$-immersed Whatman glass microfiber filter as electrolytes and separators, and Ti substrate as the current collector. Also shown in Figure 7 b and c are the galvanostatic charge–discharge and CV curves. The specific capacitances (*C*) of all samples were calculated by using Equation (2):

$$C = I/[m(\Delta V/\Delta t)] \tag{2}$$

in which *I* is the applied current, $\Delta V/\Delta t$ is the slope of the discharge curve, and *m* is the mass of the electrodes.[30] Accordingly, the specific capacitance of RuO$_2$/IL-RGO SCs was measured to be 149 F g^{-1}, which is higher than that of RuO$_2$/RGO SC (128) and IL-RGO SC (119 F g^{-1}). Despite the pseudocapacitive behavior of RuO$_2$/RGO SCs, their lower specific capacitance compared to that of RuO$_2$/IL-RGO SCs was attributed to the interaction of ILs with RGO and RuO$_2$ and different crystalline structures of RuO$_2$. This finding elucidates that the control in the crystalline structure of RuO$_2$ decorated on the RGO sub-
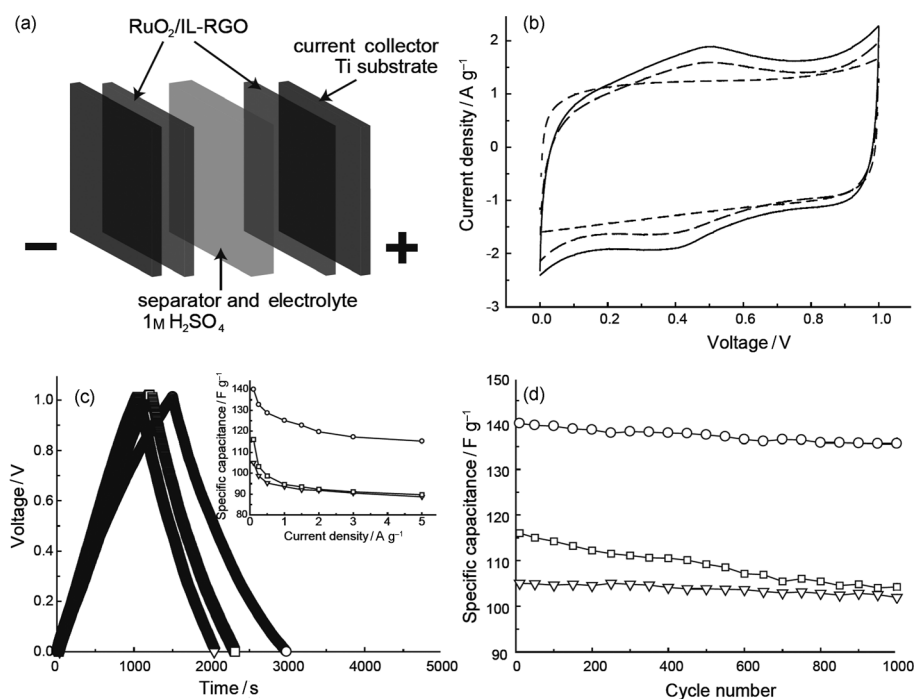
Figure 7. a) Diagram of RuO_2/IL-RGO-based SCs. b) CV curves of RuO_2/IL-RGO SC (——), RuO_2/RGO SC (– – –), and IL-RGO SC (- - - -) at a scan rate of 10 mV s^{-1}. c) Galvanostatic charge–discharge curves (inset are specific capacitances obtained at current densities of 0.1, 0.25, 0.5, 1, 1.5, 2, 3, and 5 A g^{-1}, respectively.) and d) long-term cycling stabilities of RuO_2/IL-RGO SC (○), RuO_2/RGO SC (□), and IL-RGO SC (△) at 100 mA g^{-1}.

^{2} (Figure 8a), whereas q_T^* can be evaluated from the extrapolation of q^* to $v=0$ from the plot of $1/q^*$ vs. $v^{1/2}$ (Figure 8b). q_i^* can be calculated from the difference between q_T^* and q_o^*. The ratio of q_o^*/q_T^* for RuO_2/IL-RGO hybrids (0.95) was higher than that of RuO_2/RGO hybrids (0.65). This result demonstrates that the ILs at the interface between the RGOs and RuO_2 facilitated the access of ions to the surface of RuO_2/IL-RGO hybrids and then promoted the electron transfer reactions during the charge–discharge reactions.[29,31,32]

Conclusions

We have demonstrated the facile synthesis of nanostructured electrodes, integrated with NPs and RGOs, suitable for high performance electrocatalysts (energy conversion) and pseudocapacitive materials (energy storage). The synthetic method devised herein is versatile for use with various NPs including Au, Pt, Pd,
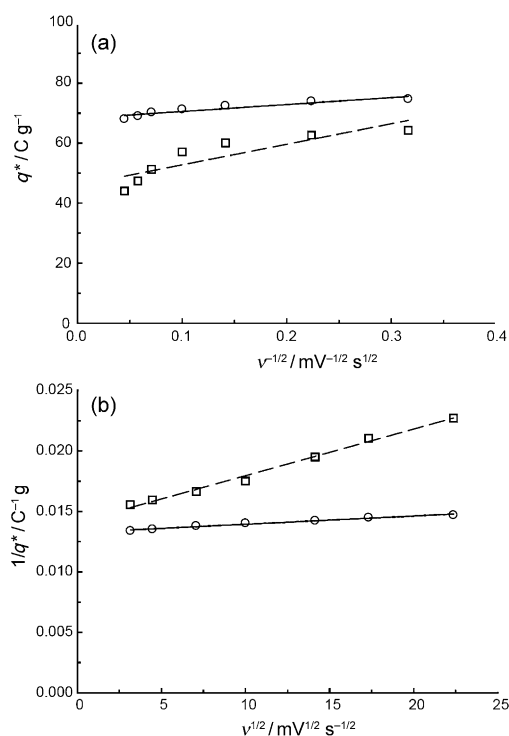
strate is crucial for improving the energy storage of SCs. Pseudocapacitive crystalline materials give rise to low-cycle SCs; hence, to confirm the cycle stability of IL-RGO SCs, galvanostatic charge–discharge tests of up to 1000 cycles were analyzed along with the galvanostatic charge–discharge curves. Crystalline RuO_2/RGO- and IL-RGO-based SCs were used as a control sample to verify the influence of RuO_2 and ILs on the capacitor performance. At a scan rate of 10 mV s^{-1}, RuO_2/IL-RGO and RuO_2/RGO SCs showed redox peaks contributing to the pseudocapacitance of RuO_2, whereas IL-RGO SCs exhibited only electrical double layer capacitance. This result was consistent with stability tests owing to intrinsic mechanical and chemical deformation; RuO_2/IL-RGO SCs retained 97% of maximum specific capacitance, which is close to that of EDLC-type RGO-based SCs, even after 1000 cycles of charge–discharge cycles. In contrast, RuO_2/RGO revealed the typical trend of pseudocapacitive materials, giving rise to a reduction of specific capacitance (89% retention) during 1000 cycles. It is evident that nanoscale hybridization of IL-RGO and RuO_2 led to synergistic effects, high specific capacitances and cycle stabilities because of the well-defined structure of RuO_2 and the interaction of ILs.

To interpret the enhancement of capacitive performance of RuO_2/IL-RGO, the ion diffusion behavior of the RuO_2/IL-RGO and RuO_2/RGO hybrids was investigated (Figure 8). On the basis of previous reports by Trasatti et al.,[31,32] the stored total charge (q_T^*) is composed of the outer charge (q_o^*) related to more accessible active surface and the inner charge (q_i^*), corresponding to less accessible active surface. q_o^* can be obtained from the extrapolation of q^* to $v=\infty$ from a plot of q^* vs. $v^{-1/}$

Figure 8. Linear extrapolation of a) q^* to $v=\infty$ and b) q^* to $v=0$ for RuO_2/IL-RGO (○) and RuO_2/RGO (□) electrodes. The dashed and continuous straight lines correspond to the respective linear regressions.

Ru, and RuO$_2$ and can be used to tune the size, amount, and crystalline structures of discrete NPs. The excellence of the resulting NP/IL-RGO hybrids has been illustrated by applications in methanol oxidation and supercapacitors, giving rise to enhanced methanol oxidation and pseudocapacitance. For the electrocatalysts, Pt/IL-RGO show larger ESAs and give rise to 43% and 63% higher efficiencies for methanol oxidation than those of Pt-RGO and E-tec, respectively. For the supercapacitors, RuO$_2$/IL-RGO, prepared through simple thermal treatment of Ru/IL-RGO, reveals higher specific capacitance and cycle stability compared to RuO$_2$/RGO and IL-RGO. These results have been attributed to the well-defined nanostructure of NPs and the favorable interaction at the interface. These materials have an important and immediate impact on energy conversion and storage as well as the related electrochemical systems.

Experimental Section

Synthesis of GOs

Graphene oxides (GOs) were prepared from graphite powder (Sigma–Aldrich, < 20 μm) by using the modified Hummer method.[19] In brief, graphite powder (2 g) was added to H$_2$SO$_4$ (10 mL) at 85 °C, and then the mixture was continuously stirred for 5 h to yield the pre-oxidized graphite, which was then mixed with K$_2$S$_2$O$_8$ (2 g) and P$_2$O$_5$ (2 g). At the end of the reaction, the resultant mixture was cooled to room temperature, washed with deionized (DI) water in a filter, and dried overnight under vacuum at room temperature. The as-obtained product was put into a cold H$_2$SO$_4$ solution (100 mL, 98 wt%), and KMnO$_4$ (10 g) was slowly added over 1 h with continuous stirring and cooling in an ice-water bath. The mixture was heated at 30 °C for 5 h in a stirred system and further stirred for 24 h at room temperature. The reaction was then terminated by addition of DI water (500 mL) and 30% H$_2$O$_2$ (20 mL), turning the color of the mixture from dark brown to bright yellow. The resulting mixture was filtered with a membrane and washed with an aqueous HCl solution (1 L, 10 wt%) to remove residual oxidant and metal ions. The resulting mixture was further washed with a large volume of DI water until pH was neutral. The filter cake was redispersed in DI water and purified by means of dialysis against water to completely remove impurities. After the purified GO was filtered, the solid product was dried and stored at 60 °C in a vacuum oven. Prior to preparation of the IL-RGO, the dried GO (5 mg) was dispersed in DI water (10 mL) by using an ultrasonic system (Fisher Scientific Model 500 ultrasonic, 350 W) for 30 min to obtain the fully exfoliated GOs.

Syntheses of IL-RGO and NP/IL-RGO hybrids

An aqueous solution of exfoliated GOs (0.5 mg mL^{-1}) was mixed with 1-butyl-3-methylimidazolium tetrafluoroborate ([bmim][BF$_4$], 0.5 mg) and immediately stirred for 30 min. This mixture was treated with a bath-type sonicator for 1 h to obtain a highly homogeneous solution of IL-GOs. After the reduction of the mixture with hydrazine (100 μL, 35 wt% in water, Aldrich), a homogeneous black dispersion of IL-RGOs was obtained. The resulting mixture was purified by means of filtration and dialysis for one week to remove excess [bmim][BF$_4$] and residual hydrazine, and then dried overnight under vacuum at 60 °C. To obtain the Pt/IL-RGO hybrids, the IL-RGO hybrids (1 mg) and H$_2$PtCl$_6$ (2×10^{-3} mmol) were added to a mixture of DI water (2 mL) and ethanol (2 mL) and sonicated in

an ultrasonicator for 3 min under controlled conditions. The as-obtained Pt/IL-RGO hybrids were purified by means of dialysis, filtered, and dried at 60 °C under vacuum. Various NP/IL-RGO hybrids were prepared through procedures identical to the preparation of IL-RGO/Pt by controlling the types of metal precursor including HAuCl$_4$·3H$_2$O, Pd(C$_2$H$_3$O$_2$)$_2$, RuCl$_3$·H$_2$O. To prepare pseudocapacitive hybrids, Ru/IL-RGO hybrids were annealed in air at 200 °C for 2 h to yield RuO$_2$/IL-RGO hybrids.

Fabrication of Pt/IL-RGO hybrid electrode

The electrocatalytic activity of Pt/IL-RGO hybrids for energy conversion was investigated by using a conventional three-electrode electrochemical cell using a Pt/IL-RGO catalyst-modified glassy carbon disk as a working electrode, a KCl-Ag/AgCl reference electrode, and a Pt wire counter electrode. The working electrode was fabricated by casting Nafion-impregnated catalysts onto a glassy carbon disk electrode. Prior to the surface modification, glassy carbon electrodes were pre-treated by polishing with alumina powders (0.05 μm), and cleaned with DI water through ultrasonication, and dried at room temperature. Pt/IL-RGO hybrids (5 mg) were ultrasonically dispersed in a 2-propanol (2 mL)-containing Nafion solution (5 wt%, DuPont) for 30 min. An aliquot (10 μL) of Pt/IL-RGO hybrid solution was drop cast onto the glassy carbon electrode and allowed to dry at room temperature.

Fabrication of RuO$_2$/IL-RGO hybrid-based supercapacitor

Electrocapacitive properties of RuO$_2$/IL-RGO hybrids for energy storage were investigated in a two-electrode system. The electrodes were prepared by modification of Cu foil as current collector with a mixture of RuO$_2$/IL-RGO hybrids and polytetrafluoroethylene (PTFE, 10 wt%) binder. A Whatman glass microfiber filter was used as the separator, containing H$_2$SO$_4$ (1 M). The supercapacitor devices were assembled using two RuO$_2$/IL-RGO-modified Ti substrates separated by the aqueous-electrolyte-soaked separator. As-obtained supercapacitor devices were dried at room temperature before the performance measurements of the devices.

Characterization

TEM measurements were performed by using a JEM-2100F HR-TEM at an acceleration voltage of 200 kV. An STEM was operated with a probe focused to 0.2 nm and camera length of 20 cm. The scan raster was 512×512 points with a dwell time of 8.5 seconds per scan. Chemical analysis was performed using a VG Electron Spectroscope (ESCA 2000) at high vacuum (10^{-10} torr) equipped with monochromater (quartz), twin X-ray source (Mg/Al target) and hemispherical analyzer. SEM images were obtained by using a field emission scanning electron microscope (FEI Sirion model) equipped with an in-house Schottky emitter in high stability. XRD data were obtained by using a Rigaku D/max IIIC (3 kW) with a q/q goniometer equipped with a CuK$_\alpha$ radiation generator. The diffraction angle of the diffractograms was in the range of $2\theta = 2$–90°. XPS data were obtained by using a VG multilab 2000 (Thermo VG Scientific) with a monochromatic MgK$_\alpha$ X-ray source ($hv = $ 1253.6 eV) in an analysis chamber at 1.33 μPa vacuum. The high resolution scans of C1s were analyzed for each sample at at least two separated locations. FTIR spectra were collected by using a JASCO FT-IR 470 plus. Each spectrum was recorded from $\tilde{v} = $ 4000 to 50 cm^{-1} using 30 scans at a resolution of 4 cm^{-1}. Cyclic voltammograms were analyzed by using a CHI 760D electrochemi-

cal workstation (CH Instruments). Galvanostatic charge–discharge measurements were carried out by using a Solartron 1260 at RT.

[1] A. S. Aricò, P. Bruce, B. Scrosati, J.-M. Tarascon, W. V. Schalkwijk, *Nat. Mater.* **2005**, *4*, 366 – 377.

[2] C. Liu, F. Li, L.-P. Ma, H.-M. Cheng, *Adv. Mater.* **2010**, *22*, E28 – E62.

[3] R. Liu, J. Duay, S. B. Lee, *Chem. Commun.* **2011**, *47*, 1384 – 1404.

[4] P. G. Bruce, B. Scrosati, J.-M. Tarascon, *Angew. Chem.* **2008**, *120*, 2972 – 2989; *Angew. Chem. Int. Ed.* **2008**, *47*, 2930 – 2946.

[5] J. Chen, F. Cheng, *Acc. Chem. Res.* **2009**, *42*, 713 – 723.

[6] B. G. Choi, H. S. Park, T. J. Park, M. H. Yang, J. S. Kim, S.-Y. Jang, N. S. Heo, S. Y. Lee, J. Kong, W. H. Hong, *ACS Nano* **2010**, *4*, 2910 – 2918.

[7] B. G. Choi, J. Hong, Y. C. Park, D. H. Jung, W. H. Hong, P. T. Hammond, H. S. Park, *ACS Nano* **2011**, *5*, 5167 – 5174.

[8] M. Pumera, *Energy Environ. Sci.* **2011**, *4*, 668 – 674.

[9] D. Wei, Y. Liu, *Adv. Mater.* **2010**, *22*, 3225 – 3241.

[10] Y. Sun, Q. Wu, G. Shi, *Energy Environ. Sci.* **2011**, *4*, 1113 – 1132.

[11] H. S. Park, B. G. Choi, S. H. Yang, W. H. Shin, J. K. Kang, D. Jung, W. H. Hong, *Small* **2009**, *5*, 1754 – 1760.

[12] F.-A. He, J.-T. Fan, F. Song, L.-M. Zhang, H. L.-W. Chan, *Nanoscale* **2011**, *3*, 1182 – 1188.

[13] T. Fukushima, A. Kosaka, Y. Ishimura, T. Yamamoto, T. Takigawa, N. Ishii, T. Aida, *Science* **2003**, *300*, 2072 – 2074.

[14] T. Fukushima, T. Aida, *Chem. Eur. J.* **2007**, *13*, 5048 – 5058.

[15] H. S. Park, J.-S. Kim, B. G. Choi, S. M. Jo, D. Y. Kim, W. H. Hong, S.-Y. Jang, *Carbon* **2010**, *48*, 1325 – 1330.

[16] X. Zhou, T. W. Wu, K. Ding, B. Hu, M. Hou, B. Han, *Chem. Commun.* **2010**, *46*, 386 – 388.

[17] H. Yang, C. Shan, F. Li, D. Han, Q. Zhang, L. Niu, *Chem. Commun.* **2009**, 3880 – 3882.

[18] S. Guo, S. Dong, E. Wang, *Adv. Mater.* **2010**, *22*, 1269 – 1272.

[19] W. S. Hummers, R. E. Offeman, *J. Am. Chem. Soc.* **1958**, *80*, 1339.

[20] Y. Xu, H. Bai, G. Lu, C. Li, G. Shi, *J. Am. Chem. Soc.* **2008**, *130*, 5856 – 5857.

[21] J. Wang, H. Chu, Y. Li, *ACS Nano* **2008**, *2*, 2540 – 2546.

[22] D. Cai, M. Song, *J. Mater. Chem.* **2007**, *17*, 3678 – 3680.

[23] S. Guo, S. Dong, E. Wang, *ACS Nano* **2010**, *4*, 547 – 555.

[24] F. Su, Z. Tian, C. K. Poh, Z. Wang, S. H. Lim, Z. Liu, J. Lin, *Chem. Mater.* **2010**, *22*, 832 – 839.

[25] L. Cao, F. Scheiba, C. Roth, F. Schweiger, C. Cremers, U. Stimming, H. Fuess, L. Chen, W. Zhu, X. Qiu, *Angew. Chem.* **2006**, *118*, 5441 – 5445; *Angew. Chem. Int. Ed.* **2006**, *45*, 5315 – 5319.

[26] Z. Q. Tian, S. P. Jiang, Y. M. Liang, P. K. Shen, *J. Phys. Chem. B* **2006**, *110*, 5343 – 5350.

[27] D. Chen, L. Tang, J. Li, *Chem. Soc. Rev.* **2010**, *39*, 3157 – 3180.

[28] K.-H. Chang, C.-C. Hu, C.-Y. Chou, *Chem. Mater.* **2007**, *19*, 2112 – 2119.

[29] Z.-S. Wu, D.-W. Wang, W. Ren, J. Zhao, G. Zhou, F. Li, H.-M. Cheng, *Adv. Funct. Mater.* **2010**, *20*, 3595 – 3602.

[30] T. Y. Kim, H. W. Lee, M. Stoller, D. R. Dreyer, C. W. Bielawski, R. S. Ruoff, K. S. Suh, *ACS Nano* **2011**, *5*, 436 – 442.

[31] D. Baronetto, N. Krstajić, S. Trasatti, *Electrochim. Acta* **1994**, *39*, 2359 – 2362.

[32] S. Ardizzone, G. Fregonara, S. Trasatti, *Electrochim. Acta* **1990**, *35*, 263 – 267.